Journal of Materials Chemistry A

ROYAL SOCIETY OF CHEMISTRY

PAPER

View Article Online
View Journal

Cite this: DOI: 10.1039/d5ta07860a

Impact of vapor phase Ge incorporation and reaction pathways on the performance and stability of $Cu_2Zn(Ge,Sn)Se_4$ solar cells

Talat Khonsor, *[abc] David Nowak,[c] Devendra Pareek,[c] Maxim Guc, [b] Robert Fonoll-Rubio,[b] Victor Izquierdo-Roca, [b] Pedro Vidal-Fuentes [b] and Levent Gütay [c]

In this study, we investigate how variations in precursor composition and partial vapor-assisted substitution of Sn by Ge affect the material quality and device performance of CZTGSe solar cells. Precursor films with different Cu–Sn alloy ratios were selenized under controlled $SnSe_{2-x}$ and $GeSe_{2-x}$ vapor conditions, enabling the synthesis of $Cu_2ZnSn_{1-x}Ge_xSe_4$ absorber layers with Ge/(Ge + Sn) ratios ranging from 0 to 36%. Despite the initial variations, the final absorber compositions converged due to in-process shifts driven by Sn and/or Ge incorporation and loss during the reaction. Beyond the established role of the absorber composition, we show that the reaction pathway, determined by the precursor composition, strongly influences the defect concentration, material quality, and device performance. A Cu-rich and Sn-poor (Cu/Sn > 2) starting composition that evolves into a Cu-poor Sn-rich kesterite absorber is found to be particularly beneficial. Furthermore, prolonged post deposition treatment revealed distinct stability trends: Ge-free devices degraded steadily, whereas Ge-containing devices continued to improve over ~430 hours. We attribute this to stabilization of [V_{Cu} + Zn_{Cu}] defect clusters and re-distribution of Ge atoms. The best-performing device, with Ge/(Ge + Sn) = 9% achieved 12.5% efficiency with enhanced long-term stability, underscoring the potential of vapor-phase Ge integration for advancing physically synthesized kesterite solar cells.

Received 25th September 2025
Accepted 21st February 2026

DOI: 10.1039/d5ta07860a

rsc.li/materials-a

Introduction

The emergence of copper zinc tin sulfide/selenide (CZTSSe) thin-film solar cells represents a significant advancement in the pursuit of sustainable, resource-saving and scalable photovoltaic technologies. While various thin-film solar cells share advantages such as lightweight, short energy payback time, and cost-effective fabrication, CZTSSe stands out due to its composition of earth-abundant, non-toxic elements, its high absorption coefficient exceeding 10^4 cm^{-1},[1,2] and its tunable band gap ranging from 1.0 to 1.85 eV through elemental substitution (*e.g.*, Sn–Ge and S–Se).[3] Despite reaching a power conversion efficiency of 12.6% early in 2013,[4] kesterite solar cell efficiencies stagnated for nearly a decade. However, recent advances have pushed the certified record efficiency of CZTSSe to 15.1%,[5] and to 14.9% with Li and Ag co-doping,[6] thereby renewing interest in this material system. Theoretically, CZTSSe holds considerable potential,[7,8] although the complex nature of quaternary kesterite compounds continues to challenge efforts to close the gap between theoretically predicted and achieved performance.

In high-performance CZTSSe devices, the attained open-circuit voltage (V_{oc}) typically reaches less than 65% of its theoretical maximum, whereas the short-circuit current (I_{sc}) and fill factor (FF) can achieve up to 85% of their respective theoretical limits.[7,9] The open-circuit voltage deficit ($V_{oc\text{-}def.}$), defined as the difference between the theoretically achievable voltage and the measured V_{oc} ($V_{oc\text{-}def.} = (E_g/q) - V_{oc}$), is widely recognized as the primary bottleneck limiting kesterite solar cell performance.[10–13] Extensive research has attributed this deficit to several contributing factors[13–24] including:

- Limited phase stability in CZTSSe, which promotes the coexistence of detrimental secondary and ternary phases that act as recombination centers and affect electrical conductivity.[16,17]
- Cu/Zn disorder, promoted by the comparable size of the Cu and Zn cations, has a critical influence on fundamental materials properties (like lattice parameters and band gap) resulting in many cases in strong microscopic fluctuations.[23,24]
- Off-stoichiometric compositions used to induce p-type conductivity often result in the formation of native point defects

[a]Electronic Engineering Department, Polytechnic University of Catalonia (UPC), 08034 Barcelona, Spain. E-mail: talat.khonsor@upc.edu
[b]Catalonia Institute for Energy Research (IREC), Jardins de les Dones de Negre 1, 2[a] pl., 08930 Sant Adrià del Besòs, Barcelona, Spain
[c]Institute of Physics, Carl von Ossietzky University of Oldenburg, Carl-von-Ossietzky Straße 9-11, 26129 Oldenburg, Germany

(vacancies, antisites, and interstitials), reducing the carrier lifetime.[17]

• The formation of a thick $MoSe_2$ layer at the back interface can hinder hole collection at the Mo back contact.[18–20]

• A high density of interface defects, particularly at the absorber–buffer junction, and unfavorable band alignment exacerbate recombination losses.[21,22]

A thorough understanding and effective control of these factors are essential for suppressing recombination pathways and improving kesterite performance. Several studies[25–27] have explored how the final absorber composition correlates with defects, secondary phases and device performance. However, this strategy is constrained by the narrow optimal composition window for CZTSSe absorbers.[28,29]

In our previous work,[30,31] we pursued an alternative strategy: rather than focusing solely on the final absorber composition, we investigated the influence of the precursor starting composition and the composition shifts during the selenization process and absorber formation on the properties of the final absorber. Using this approach, we demonstrated that despite starting from varied precursor compositions, it is possible to obtain absorbers with comparable final compositions, which, however, result in devices with different performances. The growth routes rely on the supply of $SnSe_{2-x}$ vapor during the reactive annealing step, and the incorporation and/or loss of Sn at the solid–vapor interface, which depends on the balance of the two Sn concentrations in the layer and in the vapor environment. Our results in ref. 30 demonstrated that variations in both the initial precursor composition and the formation pathway influence defect clusters and device properties, even when the final absorber compositions appear similar.

Beyond compositional tuning, elemental substitution has been widely explored to mitigate performance-limiting mechanisms. Partial replacement of Sn by Ge has been shown to reduce the formation of recombination-inducing defects (*e.g.*, Cu_{Zn}, V_{Sn}, and Sn_{Zn}), mitigate the band-tailing, and thereby improve material quality, film morphology and device performance.[11,32,33]

In this study, we extend our previous investigations on the effects of formation pathways in pure Sn-based kesterite absorbers (CZTSe) by examining the absorber formation process using a variety of precursor compositions under $SnSe_{2-x}$ and $GeSe_{2-x}$ atmospheres. The aim is to gain deeper insight into Ge incorporation *via* a vapor-assisted process and to assess how variations in in-process composition shifts affect the final absorber composition, material properties, and ultimately the optoelectronic performance of the resulting solar cell devices. Furthermore, this work evaluates the impact of prolonged low-temperature post deposition treatment (PDT) on both Ge-free and Ge-containing devices, offering insight into ageing stability and further potential pathways for material and device improvement. We hypothesize that, despite comparable final absorber composition, the reaction pathway through which this composition is achieved plays a crucial role in determining defect formation, material quality, and ultimately device performance.

Results and discussion

The study started with the preparation of a set of precursor samples. As illustrated in Fig. 1, we prepared a series of precursors with a stacking order consisting of a first layer of Zn, followed by a Cu–Sn-alloy layer, an additional layer of elemental Sn, and finally, a second Zn layer. The composition variation in the prepared precursors was achieved by adjusting the sputtering duration of the elemental Sn layer. The employed durations were 0, 40, 81, 120, 162, 243, and 324 seconds, resulting in estimated Cu/Sn ratios of 2.35, 2.20, 2.05, 1.90, 1.77, 1.55, 1.40 respectively. These composition ratios determine the alloy structure of the as-deposited Cu–Sn layer, which will be discussed in detail later. Consequently, the selenization process was conducted to form the absorbers. Within the graphite box, a specific amount of Se and Sn was evenly distributed around the sample. Meanwhile, the amount of added Ge pieces was systematically varied to ensure that each precursor composition (defined by a specific as-deposited Cu/Sn ratio) was annealed under three distinct conditions: without Ge, with a low Ge concentration, and with a relatively high Ge concentration. As a result, a complete library of samples was obtained, including samples with different Sn and Ge concentrations. In the second part of this study, we conducted a controlled post deposition soft annealing to explore the effect of this treatment on the device performance with and without Ge.

As demonstrated in previous studies by our group,[31] altering the Sn sputtering durations in the precursor Zn/CuSn/(Sn)/Zn determines the Cu/Sn ratio and influences the Cu–Sn alloy structure within the precursor. Consequently, the precursor layer contains a Cu-rich alloy (Cu_3Sn) if no additional elemental Sn is sputtered. Sputtering elemental Sn on the already sputtered Cu_3Sn layer results in gradual conversion of the Cu_3Sn alloy into a less Cu-rich, almost stoichiometric Cu_6Sn_5 alloy. However, this trend reaches a saturation point at $Cu_6Sn_5/(Cu_6Sn_5 + Cu_3Sn) \approx 0.6$ for additional Sn sputtering durations of approximately 120 to 162 s. Further sputtering of elemental Sn after this saturation region results in the presence of non-alloyed elemental Sn in the layer.[31] Despite the variation in the Cu/Sn ratio among the precursors and differences in the reactive annealing conditions, including the variation in the amount of germanium, the resulting absorbers show a convergence to similar composition regions in the ternary composition diagram (see Fig. 2).

The presence of elemental Sn wire inside the graphite box has been shown to effectively compensate for the Sn loss from the film while serving as a source of $SnSe_{2-x}$ vapor during the selenization process. As a result, this additional Sn supply induces a composition shift in the kesterite film during reactive annealing, transitioning from an initial Cu-rich/Sn-poor state (Cu/Sn = 2.35) to a final Cu-poor/Sn-rich absorber composition (Cu/Sn = 1.6).[34] In this study we introduce both Sn wire and Ge pieces into the graphite box. Since Sn and Ge atoms occupy the same sites in the kesterite crystal lattice,[35] the observed composition shift occurs not only due to the supply of $SnSe_{2-x}$ but also because of the competing $GeSe_{2-x}$ incorporation.

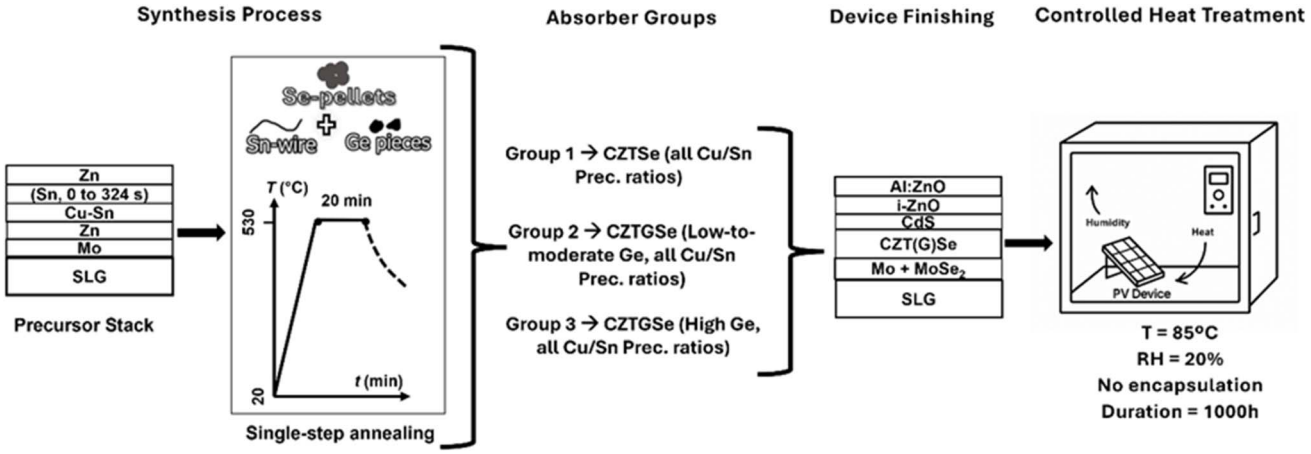

Fig. 1 Schematic illustration of the preparation of precursors with different compositions and absorbers with varying Ge/(Ge + Sn) ratios. The final part illustrates the extended post-deposition PDT.

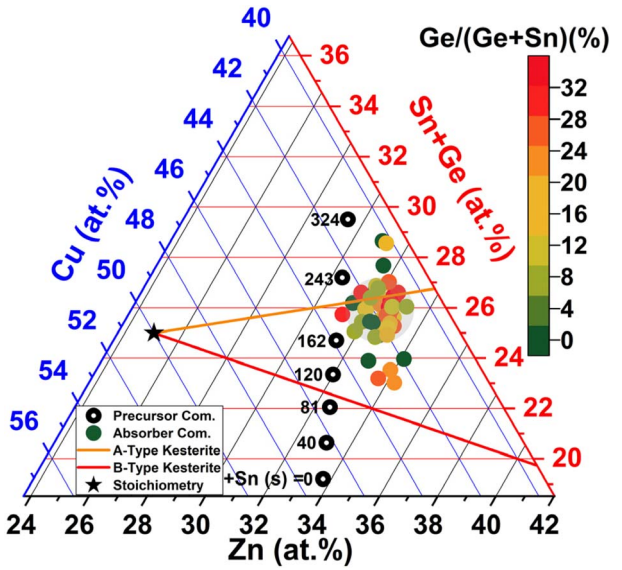

Fig. 2 Precursor composition estimated from sputtering parameters and EDX measured compositions on the absorbers (color coded according to the Ge content).

Additionally, the initial precursor composition plays a crucial role in influencing this shift. Fig. 3 illustrates the overall composition shift in CZTSe and CZTGSe for various starting precursor compositions (Cu/Sn ≈ 2.35, 2.00, and 1.40) under different reactive annealing conditions with varying Ge concentrations.

The data points shown in Fig. 3 can be classified into two cases. Case 1: CZTSe samples, in which no Ge was supplied inside the graphite box, resulting in Ge/(Ge + Sn) = 0. These samples correspond to the left-most data point in each panel. The composition shift occurs due to Sn incorporation or loss. The length and the direction of the red arrows indicate the amount of Sn incorporated or lost (downward Sn-incorporation, and upward Sn loss). Since the final absorber composition is comparable for all samples (grey region, Cu/Sn = 1.6 ± 0.1), the amount of Sn incorporated is greater for samples with initial Cu/Sn = 2.35 (Fig. 3a) than for those with Cu/Sn = 2.05 (Fig. 3b). For precursors with Cu/Sn = 1.4 (Fig. 3c), the composition shift is reversed, with Sn loss observed in the layer. This demonstrates that the amount and direction of the composition shift for the volatile species $SnSe_{2-x}$ is determined by the precursor starting composition and the balance of the amounts of $SnSe_{2-x}$ evaporating from both the sample and the additional supply inside the reaction volume (from selenized Sn wire). The Sn amount in the solid layer is determined by the balance between condensation and evaporation of $SnSe_{2-x}$ at the surface of the formed absorber film.

Case 2: CZTGSe samples, in which varying amounts of Ge are introduced into the graphite box, resulting in a Ge/(Ge + Sn) ratio ranging from 4% to 34%. Like the Cu/Sn ratio in CZTSe absorbers, the Cu/(Sn + Ge) ratio in CZTGSe-absorbers remains comparable and converges at 1.6 ± 0.1. The composition shift is influenced not only by the initial precursor composition but also by the amount of Ge supplied to the reaction volume, as well as by the competition between Ge and Sn atoms for the same lattice sites, due to the simultaneous presence of $SnSe_{2-x}$ and $GeSe_{2-x}$. In Fig. 3a, where the precursors start as highly Sn-poor/Cu-rich (Cu/Sn ≈ 2.35), a moderate Ge content (Ge/(Ge + Sn) ≈ 18%) results in a composition shift achieved partially through both Ge incorporation (downward black arrow) and Sn incorporation (indicated by a downward red arrow). At a higher Ge content (Ge/(Ge + Sn) ≈ 30%), the composition shift is dominated by Ge incorporation, as indicated by the relatively longer downward black arrow. Here no red arrow is plotted, signifying that neither Sn incorporation nor Sn loss occurs, and the Cu/Sn ratio remains unchanged between the starting precursor and the final absorber.

A similar trend is observed in Fig. 3b where the precursors start as less Sn-poor/Cu-rich, close to stoichiometry (Cu/Sn ≈ 2). However, in this case, the composition shift required to reach the final composition is smaller. For samples with Ge/(Ge + Sn) ≈ 18%, Ge incorporation alone is responsible for the entire composition shift, and no Sn incorporation is observed.

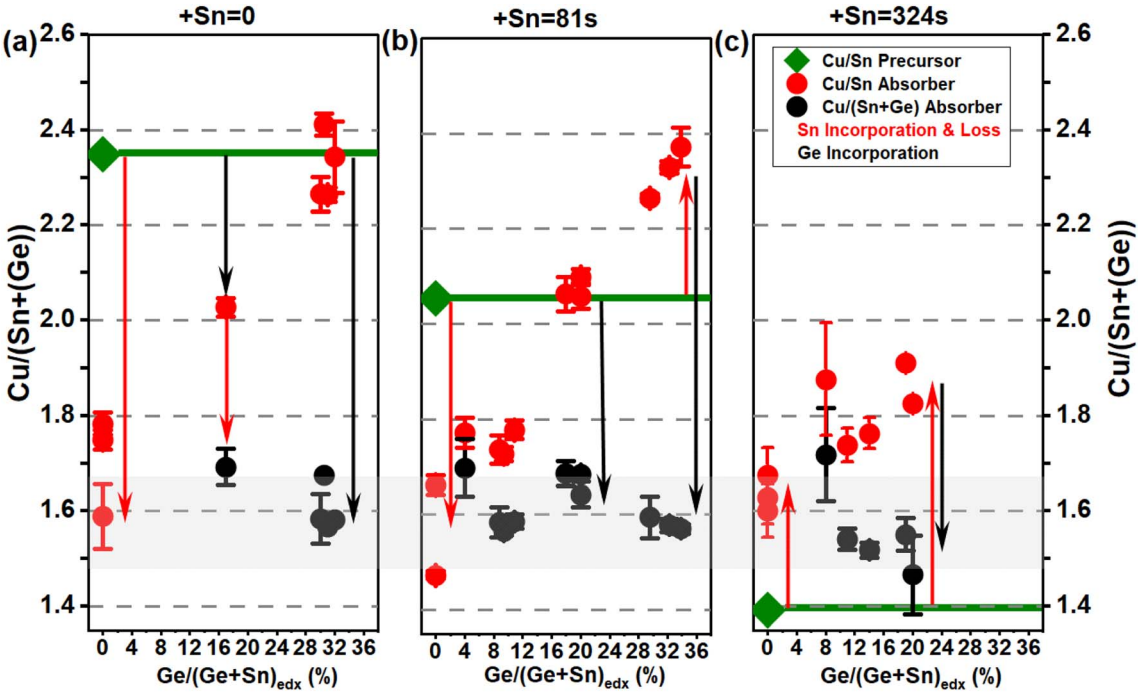

Fig. 3 Cu/Sn ratios for precursors (green) and absorbers (red), as well as Cu/(Sn + Ge) ratios for absorbers (black), plotted for each sample at a specific Ge/(Ge + Sn) ratio. The red and black arrows illustrate the shift in composition from precursors to absorbers, for Sn (red) and for Ge (black), respectively. (a) Precursors without an additional Sn layer, (b) precursors with an additional Sn layer deposited for 81 seconds, and (c) precursors with an additional Sn layer deposited for 324 seconds. A broader dataset covering all precursor compositions used in this study is provided in Fig. S1.

In the high-Ge case (Ge/(Ge + Sn) ≈ 30%), Sn loss, indicated by the upward red arrow, facilitates increased Ge incorporation into the layer. This trend is confirmed by the data shown in Fig. 3c, where the precursor starts as highly Sn-rich and Cu-poor (Cu/Sn ≈ 1.4). The observed Sn loss is further enhanced by the presence of Ge.

Our previous publications[34,36] suggest that Ge and Sn incorporate *via* similar mechanisms during selenization (governed by kinetic processes such as gas-phase transport and surface reactions). However, the observations above indicate a clear preference for Ge incorporation over Sn at the solid–vapor interface (*i.e.*, at the surface of the forming absorber film). This preference is likely due to the larger enthalpy decrease associated with $GeSe_{2-x}$ incorporation compared with $SnSe_{2-x}$.[37,38] Consequently, the previously described balance between Sn condensation and evaporation mediated by $SnSe_{2-x}$ is modified in the presence of $GeSe_{2-x}$.

The pathway by which the final absorber composition (Cu/(Sn + (Ge)) ≈ 1.6) is achieved can influence the resulting absorber properties, including the kesterite phase quality, the presence of secondary phases, and the defect concentration in the final material. Raman spectra of the bare CZTSe and CZTGSe absorbers, measured under two different excitation wavelengths (457 and 532 nm), were used to further investigate the impact of precursor composition and Ge incorporation on the resulting material characteristics.

Fig. 4a shows Raman spectra of absorbers with varying Ge content, fabricated from different precursor configurations. A $SnSe_2$ phase, identified by its Raman peak at 185 cm^{-1} (ref. 40 and 41) in Fig. 4a, is consistently observed on the surface of CZTSe absorbers grown from highly Sn-rich/Cu-poor precursors (*i.e.*, Cu/Sn 1.40). This behavior can be attributed to the highly Sn-rich growth conditions (Sn-rich precursor combined with selenization in the presence of excess $SnSe_{2-x}$ vapor), which promote the incorporation of excess Sn into the absorber layer and consequently lead to the formation of $SnSe_2$ as a secondary phase at both the surface and within the bulk. Our previous study of Ge incorporation *via* the vapor phase also revealed Sn segregation and $SnSe_2$ formation in samples with very high Ge/(Ge + Sn) ratios (<60%), resulting from the excessive substitution of Sn by Ge, which in turn increases the amount of Sn available to form $SnSe_2$.[36] This effect is not observed in the current study, because the applied Ge contents were significantly below this threshold. In summary, the formation of $SnSe_2$ may occur in our process under two conditions: either due to an extremely Sn-rich precursor composition (Cu/Sn ≈ 1.40) and/or in the presence of an excessive amount of available Ge.[28,36]

The main kesterite Raman peak (A-symmetry, commonly denoted A_1), typically located at 196 cm^{-1} for Ge-free CZTSe, shifts to a higher wavenumber upon Ge incorporation. This blueshift, arising from the substitution of Sn by Ge, has been widely reported[3,39,42] and is commonly attributed to the smaller atomic radius of Ge relative to Sn, which modifies bond lengths and thus the phonon energy. Using the empirical relation described in ref. 39, the Ge/(Ge + Sn) ratio can be estimated from the A_1 peak position. Fig. 4b compares the Ge/(Ge + Sn) ratio derived from the

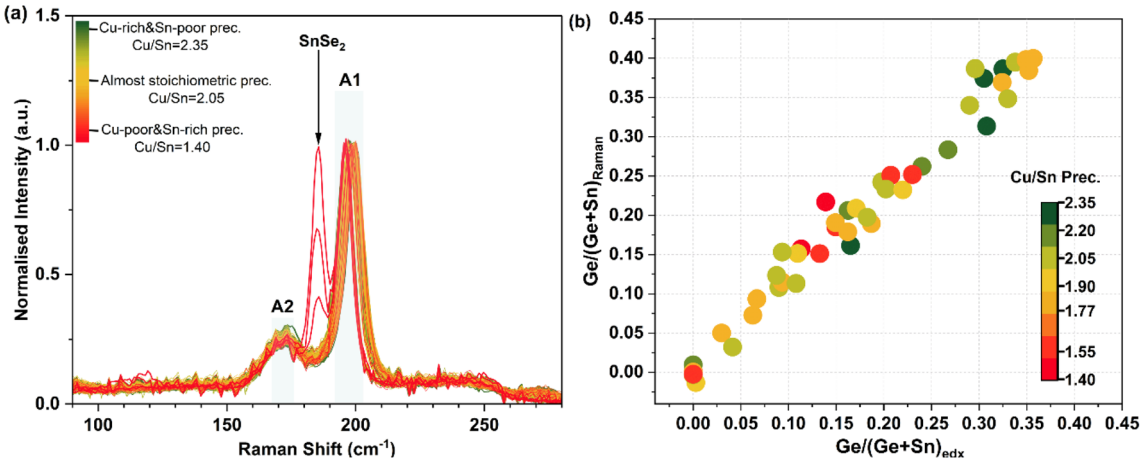

Fig. 4 (a) Raman spectra of CZT(Ge)Se absorbers measured under 532 nm excitation, normalized to the A_1 peak intensity. (b) Comparison of the estimated Ge/(Ge + Sn) ratio, calculated from the position of the main Raman kesterite peak (A_1) using the relation reported in ref. 39, with the experimentally measured Ge/(Ge + Sn) ratio from EDX.

A_1 Raman peak position $(Ge/(Ge + Sn)_{Raman})$ with the corresponding values obtained by EDX. The close agreement between both datasets indicates that the A_1 peak position is a reliable proxy for the Ge content in CZTGSe. Moreover, considering the different probing depths of Raman and EDX (Raman being more surface sensitive than EDX),[43] this agreement suggests a largely homogeneous Ge distribution throughout the absorber thickness. The slight deviation observed at higher Ge loading may reflect modest Ge enrichment near the surface. These results are consistent with our previous report on vapor-phase incorporation of Ge in CZTSe (ref. 36). The possible Ge enrichment near the surface at relatively high Ge loading can arise from the Ge supply route: Ge is introduced *via* $GeSe_2$ vapor, which initially enriches the surface before diffusing into the bulk. At elevated Ge supply, this diffusion may remain incomplete at process termination, leading to near-surface elemental enrichment, which is commonly observed in related absorber synthesis processes.[36,44,45]

A systematic broadening of the kesterite related Raman A1 peak is observed with increasing Ge content, as indicated by an increase in the full width at half maximum (FWHM) (Fig. S2). This broadening can be attributed to the expected reduction in crystalline quality caused by the incorporation of an additional element (Ge) into CZTSe, which introduces general crystal disorder and reduces the mean free path of charge carriers. However, the average change in FWHM across the solid solutions is relatively small, indicating that all thin films maintain a high degree of crystalline quality.

Raman spectra acquired using a blue excitation wavelength (457 nm) are shown in Fig. S3. These spectra reveal the presence of a ZnSe secondary phase in some samples, identified by a main peak at 250 cm^{-1}.[46] The ZnSe phase is typically observed in Zn-rich compositions $(Zn/(Ge + Sn) \approx 1.25)$ of kesterite-based absorbers, also reported in ref. 47. Introducing additional Ge *via* the vapor phase during film growth appears to reduce the formation of ZnSe, likely due to enhanced kesterite phase formation in the presence of Ge, consistent with a previous study on Ge incorporation.[48] However, due to the surface-sensitive nature of Raman spectroscopy, the observed effect of ZnSe secondary phase reduction is limited to the near surface region of the absorber film.

Another parameter commonly derived from the Raman spectra of kesterite-type compounds, which is related to the $[V_{Cu} + Zn_{Cu}]$ defect cluster concentration, is the relative integrated intensity of the A_2 peak, $I_{A_2}/(I_{A_1} + I_{A_2})$.[26,30] Fig. 5 shows this ratio

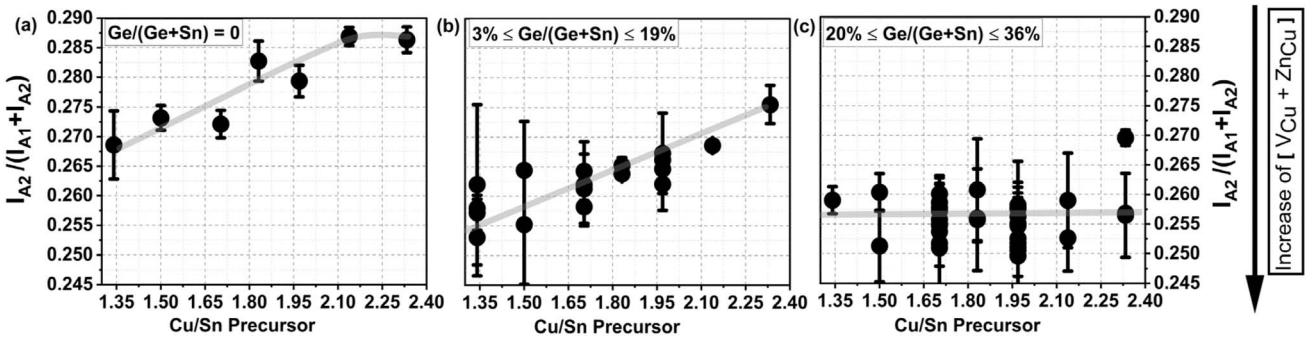

Fig. 5 Relative integrated intensity of Raman peaks of kesterite type compounds as a function of Cu/Sn ratio, based on the calculated precursor composition, for three groups of samples: (a) Ge free, (b) low-to-moderate Ge content, and (c) high Ge content. The measurements were performed at three randomly chosen points in each sample, and the average of these three measurements is shown with the standard deviation represented by error bars.

as a function of the Cu/Sn ratio in the precursor for absorbers with various Ge contents. In Ge-free samples (Fig. 5a), precursors with Cu/Sn > 1.8, which corresponds to no or only a small amount of additional Sn (Sn sputtering time <162 s), exhibit a lower $[V_{Cu} + Zn_{Cu}]$ defect cluster concentration, in agreement with the published result in ref. 26. For precursors with Cu/Sn < 1.7, a clear increase in defect cluster concentration is observed. These findings are consistent with our previous results.[30]

Samples with low to moderate Ge content (Fig. 5b) exhibit a trend similar to that of Ge-free samples, wherein $I_{A_2}/(I_{A_1} + I_{A_2})$ decreases with increasing Sn content in the precursors. This suggests comparable changes in the $[V_{Cu} + Zn_{Cu}]$ cluster concentration with variation of the Sn amount. At the same time, the presence of Ge results in an overall reduction of the observed relative integrated intensity. This difference in the absolute value of the $I_{A_2}/(I_{A_1} + I_{A_2})$ ratio may still be partially attributed to the increase in $[V_{Cu} + Zn_{Cu}]$ in these samples compared to the Ge-free absorber. However, the introduction of Ge atoms alters the bond lengths in the crystal lattice, slightly changing the vibration characteristics and thereby additionally affecting the Raman spectra and the intensity ratios between peaks.

For high Ge content (20% < Ge/(Ge + Sn) ≤ 36%, Fig. 5c), the relative integrated intensities are further reduced, and no clear trend with the Cu/Sn ratio is observable within the error bars. This suggests that a saturation level of the $[V_{Cu} + Zn_{Cu}]$ defect concentration may have been reached in this sample group due to the relatively high amount of incorporated Ge.

The impact of increasing Ge content on the $I_{A_2}/(I_{A_1} + I_{A_2})$ ratio across the full set of samples is shown in Fig. S4. A systematic decrease in this ratio with higher Ge content is observed, indicating an increase in the $[V_{Cu} + Zn_{Cu}]$ defect cluster concentration upon Ge incorporation, independent of the Cu/Sn ratio of the precursor, corroborating the preceding analysis and conclusions. Notably, the higher Ge content appears to stabilize the defect density, rendering it largely insensitive to variations in the Cu/Sn precursor composition. This is a favorable outcome for improving process reproducibility, as it minimizes the impact of small fluctuations during the precursor stage of fabrication. Later in the manuscript, we discuss how the overall increase in defect density observed in Ge-containing samples can be mitigated through post deposition treatment.

While variations in precursor composition have little effect on the absorber morphology, Ge incorporation significantly influences both grain shape and size. SEM images in Fig. 6a reveal clear morphological changes upon Ge incorporation. The polygonal and sharp-edged grains observed in pure CZTSe samples become more rounded with smoother edges, and the average grain size increases noticeably.

Fig. 6b shows the relationship between the average grain size (μm) and the Ge content, expressed as the Ge/(Ge + Sn) ratio. Grain sizes were extracted using a custom image analysis routine based on watershed clustering of SEM images. The SEM image area used for grain size estimation is shown in Fig. S5. Ge-free absorbers exhibit grain size of approximately 0.7 μm, whereas absorbers with Ge/(Ge + Sn) ≈ 40% show a significantly increased average grain size of about 1.4 μm. When considering the largest 5% of the grains, the average grain size increases from approximately 1.7 μm in Ge-free absorbers to about 3.2 μm for samples with Ge/(Ge + Sn) ≈ 40%. Grain size enlargement upon Ge incorporation has been widely reported in the literature[48–51] and is commonly attributed to the formation of a Se-rich germanium selenide (Ge_xSe_y) liquid phase during selenisation.[48–50] The presence of this liquid phase enhances elemental diffusion and promotes absorber crystallization, thereby facilitating grain growth.

Larger grains, and consequently a reduced density of grain boundaries, can in principle enhance electronic transport within the absorber layer. A beneficial correlation between increased grain size and improved device performance has been reported in several studies (*e.g.*, ref. 51).

Functional solar cell devices were fabricated from absorbers prepared with different Cu/Sn precursor ratios and varying Ge content, as described in the Experimental section. As shown in Fig. S6 nearly all devices exhibit a maximum external quantum efficiency exceeding 90%. When comparing devices fabricated from different precursor compositions (Fig. S6), no systematic trend in the EQE spectra is observed, except for samples derived from Sn-rich/Cu-poor precursors (*i.e.*, Cu/Sn < 1.55, corresponding to Sn deposition times of 243 s and 324 s), showing a noticeable reduction in the maximum achievable EQE. This degradation can be attributed to the formation of secondary phases (*e.g.*, $SnSe_2$) and an increased defect density, as inferred from the Raman analysis discussed above. A similar correlation has been reported in our previous study.[30]

Fig. 7a presents the normalized external quantum efficiency (EQE) spectra of solar cells fabricated with varying Ge content and different precursor compositions. As expected, Ge-containing samples show an increased band gap energy compared to Ge-free samples.[3,52] While the band gap of CZTSe samples remains close to 1.05 eV, it increases significantly to values above 1.25 eV for CZTGSe samples with relatively high Ge content (Ge/(Ge + Sn) ≈ 36%). Details of the band gap estimation are provided in the Supplementary Information. As shown in the upper panel of Fig. 7b, the band gap exhibits a linear dependency on the Ge/(Ge + Sn) ratio. Notably, this trend is already evident at low Ge contents (Ge/(Ge + Sn) < 12%), confirming effective substitution of Sn by Ge in the kesterite lattice.

Furthermore, by normalizing the EQE spectra and examining the shape and slope of the low-energy region in Fig. 7a, a subtle trend can be observed, suggesting a modest impact on the carrier collection length within the absorber. CZTSe-based devices show a more rectangular EQE profile compared with their CZTGSe counterparts. This difference in EQE shape suggests that Ge incorporation slightly reduces charge carrier collection, particularly for carriers generated farther from the junction. This effect is likely associated with the previously discussed increase in defect concentration and the minor reduction in crystalline quality, which can negatively affect the carrier diffusion length.

Urbach energy, extracted from EQE spectra using the procedure described in the SI, provides insights into the concentration of shallow defects.[53,54] As shown in the middle

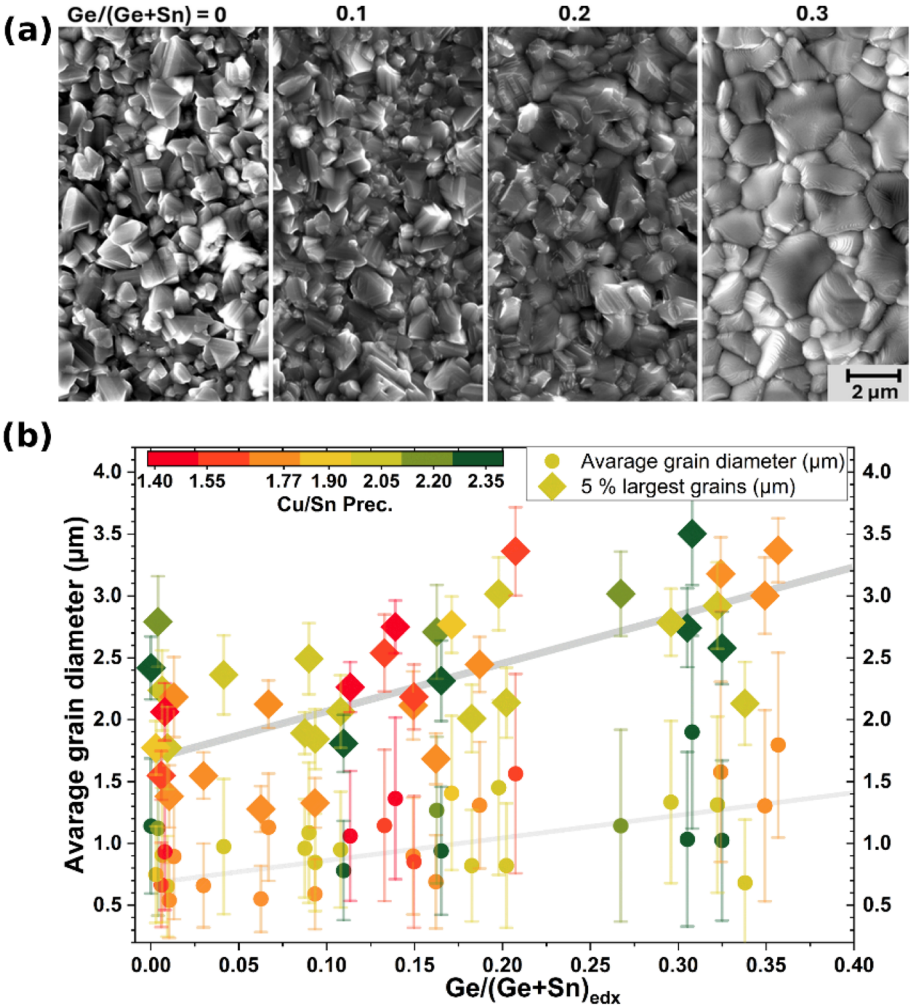

Fig. 6 (a) SEM images of sample surfaces with zero, moderate and high Ge content and (b) average grain diameter (in μm) as a function of Ge content. For each sample, three SEM images were captured at different points on the surface; the grain size in each image was estimated and averaged. Subsequently, the mean grain size across the three images was calculated for each sample and plotted, with the standard deviation of these three values included as error bars.

panel of Fig. 7b, Urbach energies in the Ge-free group are consistently below 21 meV for nearly all samples. The introduction of Ge generally leads to an increase in Urbach energy, likely reflecting the formation of additional shallow defects and an increase in overall disorder. However, for low to moderate Ge contents (Ge/(Ge + Sn) $\leq$ 20%), it is possible to obtain samples with Urbach energies comparable to those of the Ge-free group, provided the starting precursor composition is in the Sn-poor regime. In contrast, devices fabricated from Sn-rich/Cu-poor precursors (*i.e.*, Cu/Sn < 1.55) typically exhibit larger Urbach energies.

The open-circuit voltage deficit relative to the Shockley–Queisser limit ($V_{oc\text{-}def.SQ}$) was calculated using the empirical equation: $V_{oc\text{-}def.SQ} = (0.928 \times E_g/q - 0.176) - V_{oc}$. Here, the term $(0.928 \times E_g/q - 0.176)$ represents the theoretically obtainable open-circuit voltage for a given band gap, based on Shockley–Queisser assumptions.[55] For both Ge-free and Ge-containing devices with Ge/(Ge + Sn) < 12%, $V_{oc\text{-}def.SQ}$ values below 360 mV were observed (see the lower panel of Fig. 7b). In contrast, higher Ge content in the absorber results in an increased open-circuit voltage deficit for all samples, including those grown from Sn-poor precursors.

Fig. 8 illustrates the impact of Ge incorporation and variation in precursor composition on key device performance parameters, including open-circuit voltage (V_{oc}), short-circuit current density (J_{sc}), fill factor (FF), and efficiency. Increasing Ge content results in a systematic increase in V_{oc} and a concomitant decrease in J_{sc}, primarily due to the widening of the band gap (E_g). While Ge-free samples maintain an FF of approximately 63%, Ge-containing samples exhibit a clear and systematic decline in FF with increasing Ge content, indicating a negative effect on interface quality. The V_{oc} improvement achieved through Ge incorporation does not translate into higher device efficiency, as the faster reduction in J_{sc} and FF dominates, leading to a significant efficiency drop in high-Ge devices.

The observed performance degradation at high Ge concentrations can be attributed to reduced material quality and

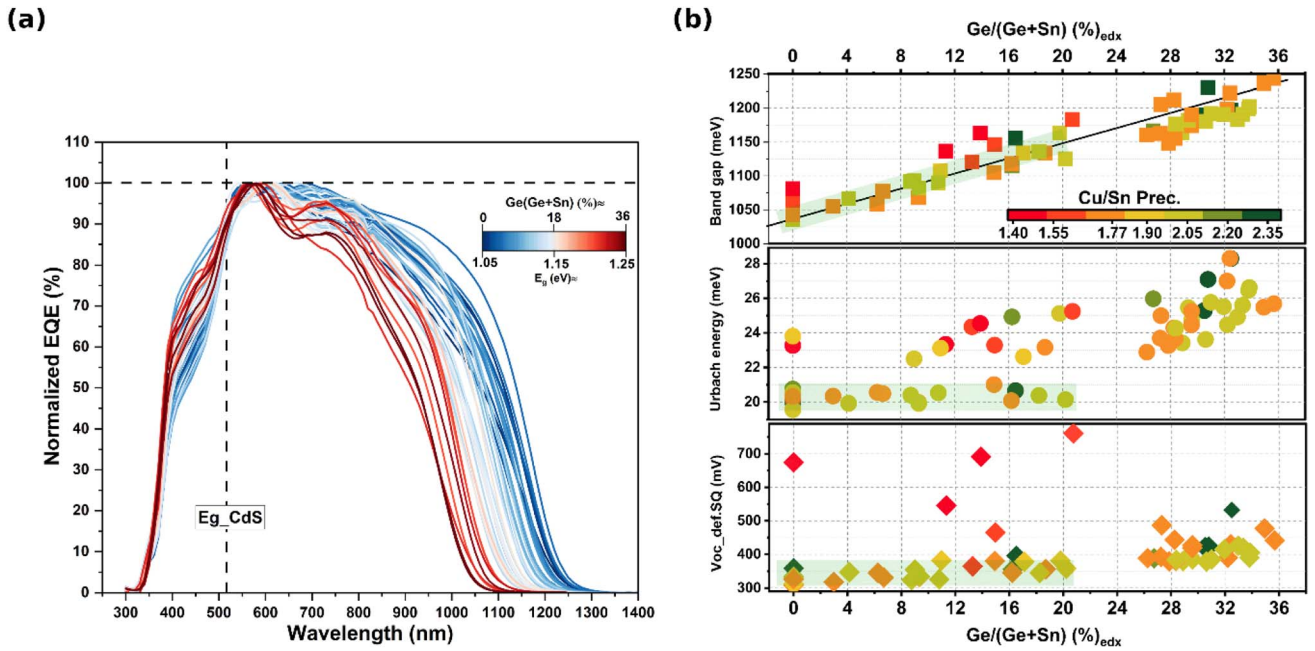

Fig. 7 (a) Normalized EQE spectra, (b) open-circuit voltage deficit relative to the Shockley–Queisser limit (lower subplot), Urbach energy (middle subplot) and band gap energy as a function of Ge content (upper subplot).

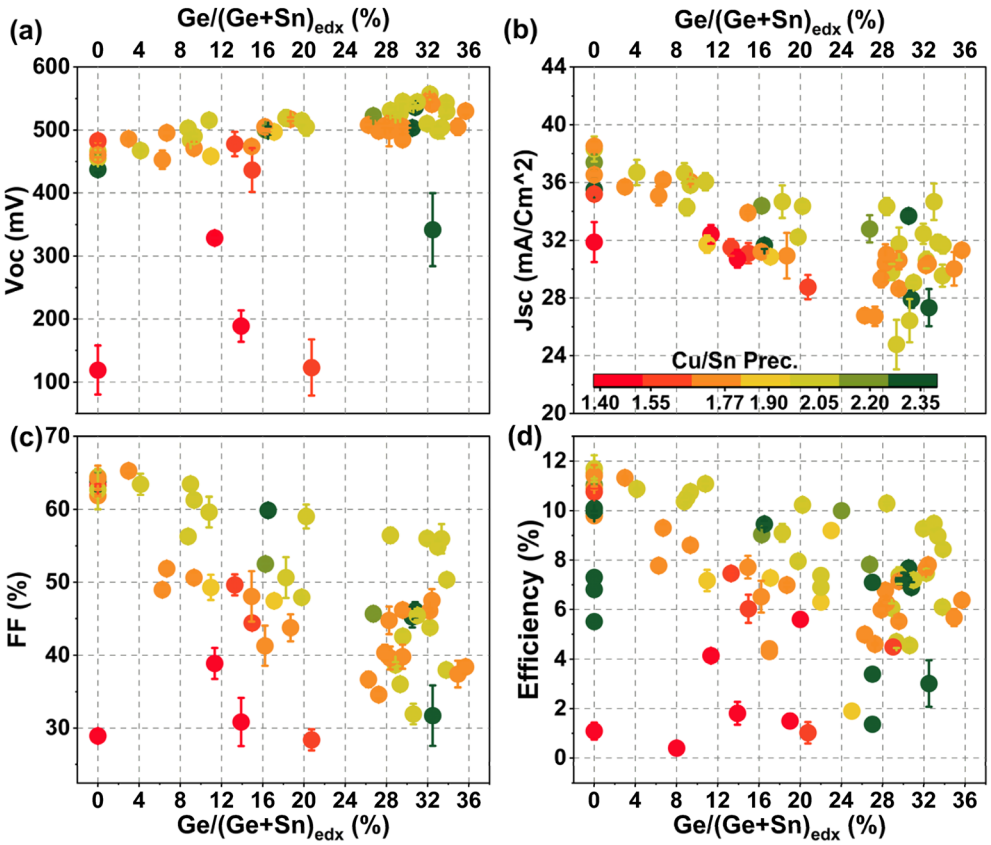

Fig. 8 Open-circuit voltage (a), short-circuit current density (b), fill factor (c), and power conversion efficiency (d) for devices fabricated from different precursor compositions, plotted as a function of Ge content. Data points are color-coded according to the Cu/Sn ratio in the precursors. Values represent the mean value of the three best-performing cells from each sample, with error bars indicating the standard deviation.

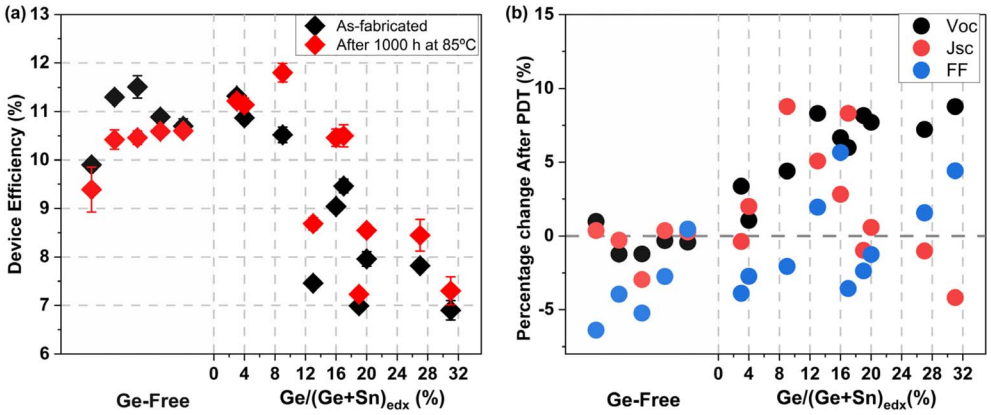

Fig. 9 (a) The measured efficiency (mean values of the best three cells in each sample) for the tested devices before and after PDT. (b) The percentage change (increase or decrease) in solar cell parameters (V_{oc}, J_{sc}, and FF) after PDT.

increased defect densities, whereas devices with low Ge content exhibit performance comparable to Ge-free devices. This is consistent with the previously discussed Urbach energy and open-circuit voltage deficit for samples with Ge/(Ge + Sn) < 12%.

Another noteworthy observation in Fig. 8 is the slightly superior performance of devices fabricated from precursors with a Cu/Sn ratio of 2.05. These precursors contain both Cu_3Sn and Cu_6Sn_5 alloys, with a $Cu_6Sn_5/(Cu_3Sn + Cu_6Sn_5)$ ratio of approximately 30%.[31] Conversely, devices prepared from Sn-rich/Cu-poor precursors (*i.e.*, Cu/Sn ≤ 1.55) exhibit pronounced performance degradation, which can be attributed to an increased concentration of point defects and secondary phases.

Post-deposition heat treatment (PDT)

In our earlier publication (ref. 36) we demonstrated that post-deposition heat treatment applied to solar cell devices with and without Ge leads to improved long-term performance for Ge containing samples, while the extended heat exposure causes a performance decrease in Ge free devices. In that study, the tested samples had a Ge/(Ge + Sn) ratio of 25%. As previously discussed, this level of Ge incorporation generally results in lower as-grown performance compared to Ge-free devices. In the present study, we extended this investigation to explore the impact of controlled PDT on devices with varying Ge content, including samples with very low Ge/(Ge + Sn) ratios, particularly below 12%, which yields as-grown performance values comparable to their Ge-free counterparts. Furthermore, several previous studies have shown and discussed the positive effect of mild post-deposition annealing (PDT) on the device performance (ref. 24 and 56).

Following our previous work,[36] and to isolate the temperature effects of the PDT process, the experiment was conducted at 85 °C and a relative humidity of 20%. These conditions were chosen to minimize humidity-induced degradation of the non-encapsulated devices and to ensure that the observed changes could be attributed primarily to temperature-related effects on device and material properties. The measurements were extended over a 1000 h period, which additionally allows comparison with stability tests reported in our previous publication (ref. 36). Current–voltage (*IV*) measurements were carried out at multiple time intervals, t = 0, 2, 5, 20, 50, 150, 200, 430, 670, and 1000 hours, on the three best-performing cells from each device. For the remaining cells in each sample, *IV* measurements were conducted only at the beginning (t = 0 h) and end (t = 1000 h) of the experiment to minimize the risk of mechanical damage from repeated probing. To evaluate the impact of the PDT on the band gab and Urbach energy, EQE measurements were carried out at both the beginning and the end of the experiment.

Fig. 9a illustrates the evolution of device efficiency following the applied PDT. While Ge-free devices exhibited a reduction in efficiency, the Ge-containing devices displayed a clear improvement. To identify the parameters responsible for these efficiency changes, the relative variations in V_{oc}, J_{sc}, and FF are shown in Fig. 9b. For the Ge-free samples, V_{oc} and J_{sc} remained essentially unchanged after PDT, whereas a reduction in FF was the primary factor contributing to the observed efficiency loss. In contrast, the Ge-containing devices exhibited a pronounced enhancement in V_{oc}, while J_{sc} remained largely unchanged or showed a slight improvement, without a consistent trend. An exception was observed for the sample with a Ge/(Ge + Sn) ratio of 31%, where a significant decrease in J_{sc} occurred. The FF of the Ge-containing devices showed a non-systematic response, with some devices exhibiting improvements and other displaying degradation.

Moreover, an opposite trend in the absorber band gap (E_g) was observed between the Ge-free and Ge-containing samples (Fig. 10, right *y*-axis, blue symbols). In Ge-free devices, E_g increased after PDT, which can be attributed to a reduction in Cu–Zn disorder and the associated improvement in structural ordering within the kesterite phase.[57,58] In contrast, the incorporation of Ge, particularly at higher Ge contents, led to a decrease in E_g. This behavior suggests that, while enhanced cation ordering tends to widen the band gap, the diffusion of Ge in Ge-containing absorbers contracts this effect, resulting in overall gap narrowing.

Despite the systematic decrease in the band gap after PDT with increasing Ge content, a substantial improvement in the measured open-circuit voltage was observed, indicating a reduction in open-circuit voltage deficit. This trend is

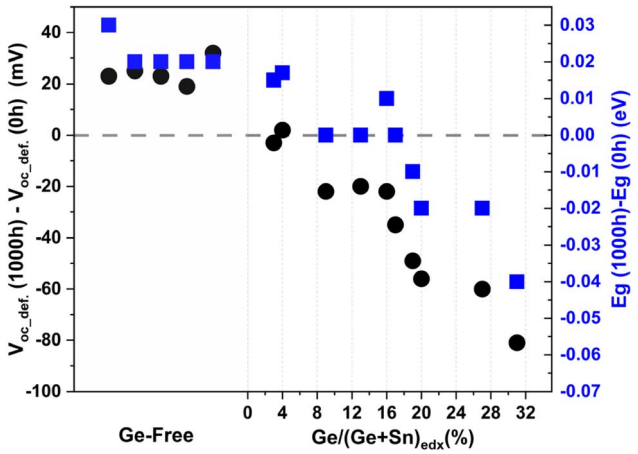

Fig. 10 The change after post-deposition PDT in open-circuit voltage deficit (black) and material band gap (blue).

corroborated in Fig. 10 (left y-axis, black symbols), which shows a clear decrease in voltage deficit with increasing Ge content. Conversely, the Ge-free samples exhibit a modest increase in voltage deficit following PDT, thereby inhibiting any gain in V_{oc} despite the widened band gap. For the Ge-containing devices, the reduction in voltage deficit following PDT enables higher V_{oc} values while simultaneously allowing potential advantages of a narrower band gaps, such as enhanced J_{sc}.

It is worth noting that the absorber and device fabrication processes were originally optimized for CZTSe-based (Ge-free) devices, which may account for the limited impact of the PDT on their performance. The observed decrease in FF in these devices is likely related to minor degradation of the window layers. In contrast, the Ge-containing devices exhibited a pronounced performance enhancement, including increases in V_{oc} and J_{sc} as well as a reduction in open-circuit voltage deficit, indicating a substantial improvement in absorber quality. To elucidate the mechanisms underlying this improvement, Urbach energies and defect-related parameters were evaluated before and after PDT, as presented in Fig. 11a and b. Consistent with the previously discussed trends, Urbach energy increased in the Ge-free devices but decreased in the Ge-containing counterparts. Since Urbach energy is sensitive to shallow defect states,[53,54] the reduction in E_u observed for Ge-containing absorbers indicates a lower defect density following PDT.

Additional evidence is provided by the change in the relative integrated Raman peak intensity, $I_{A_1}/(I_{A_1} + I_{A_2})$ (Fig. 11b), which suggests a reduction in defect cluster concentrations associated with $[V_{Cu} - Zn_{Cu}]$ defects in Ge-containing samples after PDT.

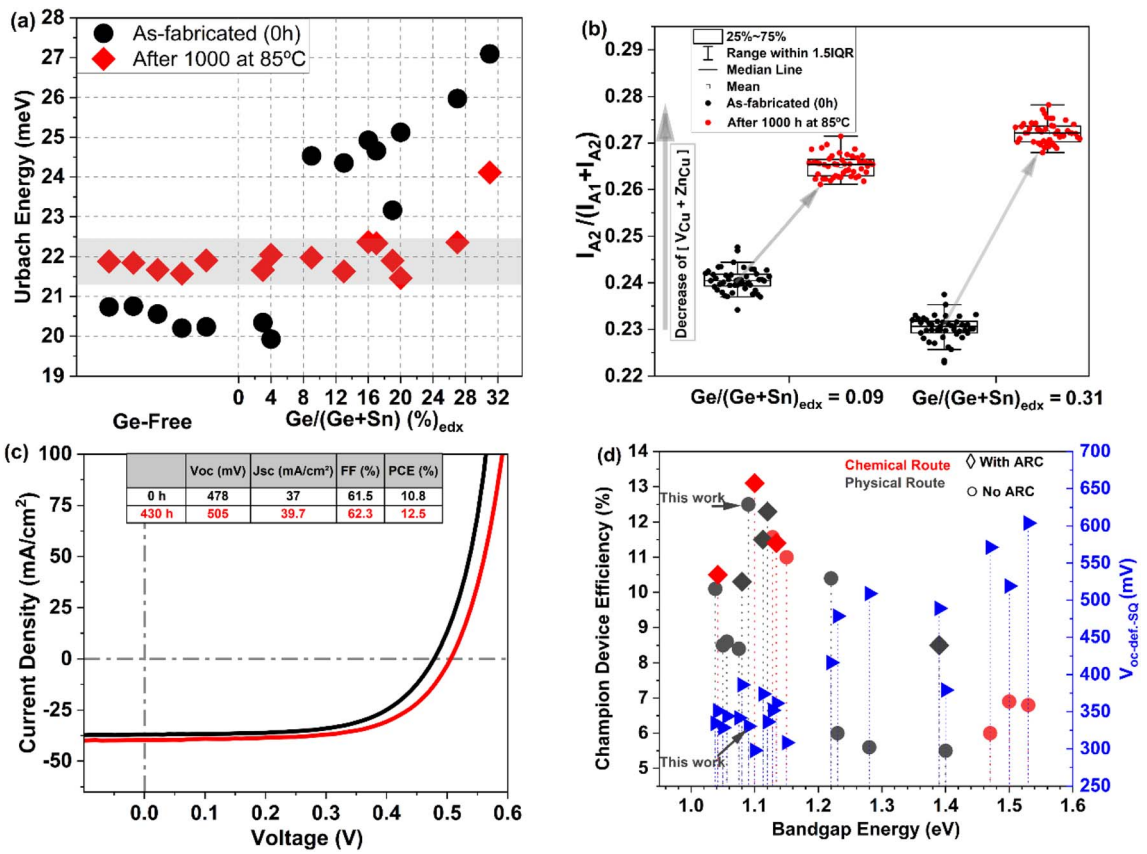

Fig. 11 (a) Comparison of Urbach energies before (0 h) and after (1000 h) PDT. (b) Raman peak integrated intensity ratios for two samples with Ge/(Ge + Sn) ratios of 9% and 31% before (0 h) and after (1000 h) PDT. (c) J–V curves of the champion device before heat treatment (0 h) and after 430 h of PDT. (d) Champion efficiency and the corresponding V_{oc} deficit relative to the SQ limit as a function of absorber band gap, compared with literature-reported values for Ge-alloyed CZTSSe absorbers (ref. 36, 51 and 59–76). ARC stands for antireflective coating.

Notably, the defect levels approach those of the Ge-free samples prior to PDT (see Fig. 5a for comparison). Taken together, the performance improvements observed in the Ge-containing devices—including reduced non-radiative recombination, diminished band tailing, and enhanced carrier collection—suggest an elemental redistribution, particularly of Ge, that promotes defect healing and mitigates localized states near the band edges.

Fig. S9 illustrates the temporal evolution of the standard solar cell parameters (efficiency, FF, J_{sc}, and V_{oc}) during prolonged PDT. For Ge-free samples, J_{sc} and V_{oc} show only minor variations throughout the experiment. In contrast, the Ge-containing samples exhibit an initial increase in J_{sc} followed by a pronounced decrease, while V_{oc} continuously increases, an effect that is more pronounced at higher Ge contents. The FF of the Ge-free samples remains close to its initial value for approximately 5 h, after which it decreases and then partially recovers. By comparison, Ge-containing devices exhibit a clear FF improvement after 2 h, which is maintained up to ~50 h. Beyond this point, FF decreases; however, by the end of the experiment it remains slightly higher than the initial value. The Ge-free samples, with an initial mean efficiency of 10.5%, maintain stable performance during the first 5 h, followed by a gradual decline to an average efficiency of approximately 9% after 200 h. A partial recovery is observed thereafter, although the final efficiency remains slightly below the initial value. In contrast, the Ge-containing devices exhibit a noticeable performance improvement after just 2 hours of treatment. This enhancement persists up to 50 h, after which some fluctuations occur. Despite a slight decline at longer treatment times, likely due to aging effects, the final efficiency of the Ge-containing devices remains higher than their initial values.

To further examine the beneficial effect observed during the early stage of post-deposition treatment in Ge-containing devices, an additional experiment was conducted. Two devices with Ge/(Ge + Sn) = 20% were subjected to separate post-deposition annealing treatments. In both cases, the annealing duration was 2 h, while the temperature was varied (85 °C for one device and 100 °C for the other). Annealing was performed in a tube furnace under a nitrogen atmosphere at atmospheric pressure. As shown in Fig. S10, both treatments led to improved performance: the mean efficiency increased from ~8.8% to ~10.5% at 85 °C and from ~9.7 to 10.8 at 100 °C. These results confirm that the initial hours of prolonged heat treatment effectively act as a mild annealing step, yielding a measurable enhancement in device performance.

In this work, the highest conversion efficiency was measured in a device with a Ge/(Ge + Sn) ratio of 9%. The initial efficiency before PDT was 10.8% and reached its highest value of 12.5% after 430 hours of PDT (slightly decreasing again for longer durations). This device was fabricated from a previously described precursor stack with an elemental Sn layer deposited for 81 s. Fig. 11c illustrates the evolution of standard solar cell parameters, including power conversion efficiency (PCE), J_{sc}, V_{oc}, and FF, along with the corresponding *J–V* curves. Fig. 11d summarizes the champion device efficiencies and the corresponding open-circuit voltage deficit relative to the SQ limit for Ge-incorporated CZT(S)Se absorbers. The highest efficiency obtained in this study represents the current record for CZTGSe fabricated by physical vapor deposition. Notably, the devices analyzed in this work do not include any antireflective coating (ARC). The application of an ARC could further enhance device performance to values comparable to the top efficiencies attained by chemical processes.

Conclusion

In this study, we investigated the growth mechanism of CZT(G)Se absorbers through various formation pathways, which were influenced by precursor composition and the availability of $GeSe_{2-x}$ during the high temperature annealing step. These pathways govern the competing incorporation dynamics of Sn and Ge, including potential Sn volatilization. Our findings indicate that when Ge is present, kesterite phase formation is predominantly facilitated by Ge rather than Sn, with externally supplied Ge atoms replacing pre-existing Sn atoms during crystallization. Although all pathways can result in absorbers with similar final Cu-poor compositions with a Cu/(Sn + Ge) ratio of approximately 1.6, the specific formation route significantly impacts material quality and device performance. Notably, growth from precursors near stoichiometric Cu/Sn ≈ 2.0 or slightly Cu-rich (Cu/Sn ≈ 2.2) exhibited superior photovoltaic characteristics in the final devices.

Ge incorporation *via* vapor phase transport proved to be a reliable method for achieving homogeneous Ge distribution. While as-fabricated CZTSe devices initially mostly outperformed their Ge-containing counterparts, post deposition PDT led to a substantial efficiency improvement in CZTGSe devices. The enhanced performance, surpassing that of Ge-free devices, is primarily attributed to improved material quality, and reduced defect concentration, resulting in a lower Urbach energy and open-circuit voltage deficit. The highest efficiency achieved in this study during the PDT experiment was 12.5% for a CZTGSe device with Ge/(Ge + Sn) = 9%, accompanied by a V_{oc} of 505 mV, J_{sc} of 39.7 mA cm^{-2}, and a FF of 62.1%.

These results position CZTGSe as a promising candidate for high-efficiency, earth abundant, band gap tunable thin film photovoltaic technology, and with higher aging stability than Ge-free CZTSe. Moreover, the demonstrated effectiveness of an industry-compatible physical vapor deposition (PVD) process underscores its potential for scalable manufacturing. Future efforts may focus on further exploring post deposition PDT for CZTGSe materials to deepen the understanding of its role in enhancing device performance.

Experimental details

Device fabrication

The SLG/Mo/CZTGSe/CdS/iZnO/Al: ZnO samples were produced on 3 mm thick Mo-coated soda lime glass substrates provided by an external partner (Zentrum für Sonnenenergie und Wasserstoffforschung Baden-Württemberg, Germany (ZSW)). Prior to absorber fabrication, an Ar^+-plasma etching cleaning step was performed (Von Ardenne cluster tool with Ar^+ ions). The

precursors were prepared by sputtering stacked elemental and alloyed layers (Zn/CuSn/(Sn)/Zn) resulting in various compositions (*i.e.*, Cu/Sn ratios). Sputtering machine: Von Ardenne cluster tool CS 400 ES, with DC magnetron sputtering. The sputtering rates were 23.7 μg s^{-1} for the Zn target, 28.8 μg s^{-1} for the Sn target and 11.2 μg s^{-1} for the Cu–Sn target. The CuSn-alloy target was composed of 64 at% copper and 36 at% tin.

Subsequently, the absorber (CZTSe or CZTGSe) was formed by a reactive annealing process conducted in a semi-closed graphite box placed within a quartz-glass conventional tube furnace (Carbolite Eurotherm 2416CG, 2416P8). The annealing parameters were kept identical for all preparation runs (base pressure: 10 mbar (N_2), heating ramp: 10 °C min^{-1}, maximum temperature: 530 °C, dwelling duration at maximum temperature: 20 min, and uncontrolled cooling by opening the furnace lid while maintaining the vacuum). In addition to the two as-sputtered precursors placed inside the graphite box, 210 ± 3 mg of selenium pellets (Mateck, 99.999 purity), 10 cm of tin wire (Alfa Aesar Puratronic, wire 0.25 mm diameter, 99.998 purity) with an approximate weight of 37 mg, and a varying amount (0–15 mg) of germanium pieces (Alfa Aesar, 99.999 purity) were evenly distributed around the two precursors. Due to the porous structure of the graphite box material, absorption and subsequent re-release of Se, Sn and Ge by the box walls are possible, potentially impacting the following process runs. Accordingly, to obtain desired Ge/(Ge + Sn) ratios in the synthesized absorber, one or more pre-conditioning runs are necessary. For synthesizing Ge-free absorbers, a second identical graphite box not contaminated with Ge was used. In each annealing run two identical absorbers were fabricated simultaneously; one of them was further fabricated as a solar cell device (buffer and window layer applied), while the second (bare absorber) was used for further characterization.

The solar cell finishing steps after obtaining the absorbers include a chemical bath deposition for depositing of a CdS layer of approximately 50 nm. The deposition of CdS was performed in a magnetically stirred chemical bath using 125.0 g of DI-water, 20 ml of 25% ammonia (NH_3), 121.2 ml of thiourea TU (concentration: 0.32 mol l^{-1}) and 5 ml cadmium-acetate CdAc (concentration: 0.0776 mol l^{-1}). The temperature of the chemical bath was set to 70 °C and the deposition duration was set to 10 minutes. The window layers used included intrinsic zinc oxide (i-ZnO) and aluminum dopped zinc oxide (Al:ZnO) layers deposited by radio frequency (RF) sputtering (the layer thicknesses were approximately 75 nm for i-ZnO and 500 nm for Al:ZnO). The sputtering parameters used were as follows: an Ar-flow of 80 sccm, a sample holder temperature of 110 C, a power of 185 W, a voltage of 200 V, and a pressure 1.6 × 10^{-3} mbar.

Each sample was then separated into nine cells by mechanical scribing, each with an approximate area of 25 mm^2. No antireflection coating was applied on any of the samples in this study.

Characterization methods

The composition of the as-sputtered precursors was calculated based on the sputtering rate, deposition duration, the atomic weight of each element, and Avogadro′s constant. The compositions of the final absorbers were determined by energy-dispersive X-ray spectroscopy (EDX) (FEI Helios 600i). EDX spectra were recorded with an acceleration voltage of 20.0 kV and a current of 1.4 × nA at 5000× magnification; for each sample an average of three independent measurements performed in different regions was calculated. Morphology and average grain sizes were determined by scanning electron microscopy SEM (FEI Helios 600i). Raman spectroscopy measurements were performed with two excitation wavelengths, 457 nm and 532 nm acquired with a commercial Raman spectrometer system (LabRam Aramis, Horiba scientific).

The external quantum efficiency (EQE) of the resulting devices was measured at room temperature in a spectral range of 300 nm to 1400 nm using a Bentham TMc300 monochromator, Quartz-Halogen and xenon lamps and a Stanford research systems SR830 DSP lock-in-amplifier. The material's band gap was extracted from the EQE^2 (E) plot (see Fig. S7). Urbach energies were obtained by a linear interpolation of the linear part below the band gap of ln (EQE (E)) plots, as explained in ref. 77 (see Fig. S8). Current–voltage characterization was performed under standard test conditions with an AAA-class sun simulator (Photo Emission Tech Inc., USA). Post-deposition soft annealing experiments were carried out in a climate chamber (Weiss Umwelttechnik GmbH, type SC 600/70). Unencapsulated devices were placed inside the chamber for a total of 1000 hours at 85 °C, with the relative humidity maintained at 20%.

Conflicts of interest

There are no conflicts to declare.

Data availability

All data supporting the findings of this study are included in the main manuscript and its supplementary information (SI). Any additional related data are available from the authors upon reasonable request. Supplementary information is available. See DOI: https://doi.org/10.1039/d5ta07860a.

Acknowledgements

This project has received funding from the European Union's Horizon 2020 research and innovation program under grant agreement no. 952982 ("Custom-Art"). Also, this work is part of the project SCALING (PID2022-138434OB-C52) funded by MCIN/AEI/10.13039/501100011033/FEDER, UE. This work is part of the project InnoPV (ref. PID2022-140226OB-C31) funded by MCIN/AEI/10.13039/501100011033/FEDER, UE. This work is part of the project CURIO-CITY (PID2023-148976OB-C42) está financiado por MCIN/AEI/10.13039/501100011033/FEDER, UE. The authors from IREC belong to the MNT-Solar Consolidated Research Group of the "Generalitat de Catalunya" (ref. 2021 SGR 0 1286) and acknowledge support from European Regional Development Funds (ERDF, FEDER Programa Competitivitat de

Catalunya 2007–2013). M. G. acknowledges the financial support from MCIN/AEI/10.13039/501100011033 and from FSE+ within the Ramón y Cajal (RYC2022-035588-I) program. T. K. thanks the Hans-Böckler-Stiftung for the scholarship and for supporting this work.

References

1 M. He, C. Yan, J. Li, M. P. Suryawanshi, J. Kim, M. A. Green and X. Hao, *Adv. Sci.*, 2021, **8**, 1–16.
2 S. Giraldo, Z. Jehl, M. Placidi, V. Izquierdo-Roca, A. Pérez-Rodríguez and E. Saucedo, *Adv. Mater.*, 2019, **31**, 1–11.
3 D. B. Khadka and J. H. Kim, *J. Phys. Chem. C*, 2015, **119**, 1706–1713.
4 W. Wang, M. T. Winkler, O. Gunawan, T. Gokmen, T. K. Todorov, Y. Zhu and D. B. Mitzi, *Adv. Energy Mater.*, 2014, **4**, 1–5.
5 M. A. Green, E. D. Dunlop, M. Yoshita, N. Kopidakis, K. Bothe, G. Siefer, D. Hinken, M. Rauer, J. Hohl-Ebinger and X. Hao, *Prog. Photovolt. Res. Appl.*, 2024, **32**, 425–441.
6 X. Zhong, J. Wang, L. Han, J. Chi, T. Liu, D. Kou, W. Zhou, Z. Zhou, S. Yuan, Y. Meng, Y. Qi, Q. Meng and S. Wu, *Adv. Funct. Mater.*, 2024, **35**, 2418548.
7 L. Grenet, M. A. A. Suzon, F. Emieux and F. Roux, *ACS Appl. Energy Mater.*, 2018, **1**, 2103–2113.
8 A. Walsh, S. Chen, S. H. Wei and X. G. Gong, *Adv. Energy Mater.*, 2012, **2**, 400–409.
9 S. Rühle, *Sol. Energy*, 2016, **130**, 139–147.
10 Y. Gong, R. Qiu, C. Niu, J. Fu, E. Jedlicka, R. Giridharagopal, Q. Zhu, Y. Zhou, W. Yan, S. Yu, J. Jiang, S. Wu, D. S. Ginger, W. Huang and H. Xin, *Adv. Funct. Mater.*, 2021, **31**, 2101927.
11 M. Ritzer, S. Schönherr, P. Schöppe, W. Wisniewski, S. Giraldo, G. Gurieva, A. Johannes, C. T. Plass, K. Ritter, G. Martínez-Criado, S. Schorr, E. Saucedo, C. Ronning and C. S. Schnohr, *ACS Appl. Energy Mater.*, 2020, **3**, 558–564.
12 C. H. M. Chuang, A. Maurano, R. E. Brandt, G. W. Hwang, J. Jean, T. Buonassisi, V. Bulović and M. G. Bawendi, *Nano Lett.*, 2015, **15**, 3286–3294.
13 J. Kim and B. Shin, *Electron. Mater. Lett.*, 2017, **13**, 373–392.
14 S. Garud, B. Vermang, S. Sahayaraj, S. Ranjbar, G. Brammertz, M. Meuris, A. Smets and J. Poortmans, *Phys. Status Solidi C*, 2017, **14**, 1700171.
15 A. Kanevce, I. Repins and S. H. Wei, *Sol. Energy Mater. Sol. Cells*, 2015, **133**, 119–125.
16 M. Kumar, A. Dubey, N. Adhikari, S. Venkatesan and Q. Qiao, *Energy Environ. Sci.*, 2015, **8**, 3134–3159.
17 N. Nln, K. Kaur and M. Kumar, *J. Mater. Chem. A*, 2020, **8**, 21547–21584.
18 J. Kim, G. Y. Kim, W. Jo, K. J. Yang, J. H. Sim, D. H. Kim and J. K. Kang, *RSC Adv.*, 2016, **6**, 103337–103345.
19 J. J. Scragg, T. Kubart, J. T. Wätjen, T. Ericson, M. K. Linnarsson and C. Platzer-Björkman, *Chem. Mater.*, 2013, **25**, 3162–3171.
20 J. J. Scragg, J. T. Wätjen, M. Edoff, T. Ericson, T. Kubart and C. Platzer-Björkman, *J. Am. Chem. Soc.*, 2012, **134**, 19330–19333.
21 K. Kaur, N. Kumar and M. Kumar, *J. Mater. Chem. A*, 2017, **5**, 3069–3090.
22 L. Yin, G. Cheng, Y. Feng, Z. Li, C. Yang and X. Xiao, *RSC Adv.*, 2015, **5**, 40369–40374.
23 W. Chen, D. Dahliah, G. M. Rignanese and G. Hautier, *Energy Environ. Sci.*, 2021, **14**, 3567–3578.
24 F. Atlan, I. Becerril-Romero, S. Giraldo, V. Rotaru, Y. Sánchez, G. Gurieva, S. Schorr, E. Arushanov, A. Pérez-Rodríguez, V. Izquierdo-Roca and M. Guc, *Sol. Energy Mater. Sol. Cells*, 2023, **249**, 112046.
25 M. Dimitrievska, F. Oliva, M. Guc, S. Giraldo, E. Saucedo, A. Pérez-Rodríguez and V. Izquierdo-Roca, *J. Mater. Chem. A*, 2019, **7**, 13293–13304.
26 M. Dimitrievska, A. Fairbrother, E. Saucedo, A. Pérez-rodríguez and V. Izquierdo-roca, *Appl. Phys. Lett.*, 2015, **106**, 073903.
27 M. Ritzer, S. Kim, S. Schorr, G. Gurieva, M. Guc and M. Dimitrievska, *J. Phys.: Energy*, 2020, **2**, 012002.
28 A. Fairbrother, M. Dimitrievska, Y. Sánchez, V. Izquierdo-Roca, A. Pérez-Rodríguez and E. Saucedo, *J. Mater. Chem. A*, 2015, **3**, 9451–9455.
29 S. Siebentritt, *Thin Solid Films*, 2013, **535**, 1–4.
30 D. Nowak, F. Atlan, D. Pareek, M. Guc, A. Perez-Rodriguez, V. Izquierdo-Roca and L. Gütay, *Sol. Energy Mater. Sol. Cells*, 2023, **256**, 112342.
31 D. Nowak, T. Taskesen, D. Pareek, T. Pfeiffelmann, U. Mikolajczak and L. Gütay, *Sol. RRL*, 2021, **5**, 2100237.
32 R. Scaffidi, G. Birant, G. Brammertz, J. de Wild, D. Flandre and B. Vermang, *J. Mater. Chem. A*, 2023, **11**, 13174–13194.
33 S. Tao, H. Wang, M. Jia, J. Han, Z. Wu, J. Zhou, M. Baranova, H. Zhu, M. Zhao and D. Zhuang, *Adv. Funct. Mater.*, 2025, **35**(23), 2423251.
34 D. Pareek, T. Taskesen, J. A. Márquez, H. Stange, S. Levcenco, I. Simsek, D. Nowak, T. Pfeiffelmann, W. Chen, C. Stroth, M. H. Sayed, U. Mikolajczak, J. Parisi, T. Unold, R. Mainz and L. Gütay, *Sol. RRL*, 2020, **4**, 2000124.
35 Y. E. Romanyuk, S. G. Haass, S. Giraldo, M. Placidi, D. Tiwari, D. J. Fermin, X. Hao, H. Xin, T. Schnabel, M. Kauk-Kuusik, P. Pistor, S. Lie and L. H. Wong, *J. Phys.: Energy*, 2019, **1**, 044004.
36 D. Nowak, T. Khonsor, D. Pareek and L. Gütay, *Appl. Sci.*, 2022, **12**, 1376.
37 T. Maeda, S. Nakamura and T. Wada, *Jpn. J. Appl. Phys.*, 2011, **50**, 04DP07.
38 S. Nakamura, T. Maeda and T. Wada, *Jpn. J. Appl. Phys.*, 2010, **49**, 121203.
39 E. Garcia-Llamas, M. Guc, I. V. Bodnar, X. Fontané, R. Caballero, J. M. Merino, M. León and V. Izquierdo-Roca, *J. Alloys Compd.*, 2017, **692**, 249–256.
40 S. Larach, R. E. Shrader and C. F. Stocker, *Phys. Rev.*, 1957, **108**, 587–589.
41 G. Lermann, T. Bischof, A. Materny, W. Kiefer, T. Kümmell, G. Bacher, A. Forchel and G. Landwehr, *J. Appl. Phys.*, 1997, **81**, 1446–1450.
42 M. Grossberg, K. Timmo, T. Raadik, E. Kärber, V. Mikli and J. Krustok, *Thin Solid Films*, 2015, **582**, 176–179.

43 J. Andrade-Arvizu, R. Fonoll-Rubio, Y. Sanchez, I. Becerril-Romero, C. Malerba, M. Valentini, L. Calvo-Barrio, V. Izquierdo-Roca, M. Placidi, O. Vigil-Galán, A. Pérez-Rodríguez, E. Saucedo and Z. Jehl Li-Kao, *ACS Appl. Energy Mater.*, 2020, **3**, 10362–10375.
44 X. Zhang, Z. Zhou, L. Cao, D. Kou, S. Yuan, Z. Zheng, G. Yang, Q. Tian, S. Wu and S. Liu, *Adv. Funct. Mater.*, 2023, **33**, 2211315.
45 T. Taskesen, D. Pareek, D. Hauschild, A. Haertel, L. Weinhardt, W. Yang, T. Pfeiffelmann, D. Nowak, C. Heske and L. Gütay, *RSC Adv.*, 2021, **11**, 12687–12695.
46 H. Li, B. Wang and L. Li, *J. Alloys Compd.*, 2010, **506**, 327–330.
47 E. Grau-Luque, I. Anefnaf, N. Benhaddou, R. Fonoll-Rubio, I. Becerril-Romero, S. Aazou, E. Saucedo, Z. Sekkat, A. Perez-Rodriguez, V. Izquierdo-Roca and M. Guc, *J. Mater. Chem. A*, 2021, **9**, 10466–10476.
48 S. Giraldo, E. Saucedo, M. Neuschitzer, F. Oliva, M. Placidi, X. Alcobé, V. Izquierdo-Roca, S. Kim, H. Tampo, H. Shibata, A. Pérez-Rodríguez and P. Pistor, *Energy Environ. Sci.*, 2018, **11**, 582–593.
49 C. Gao, Y. Sun and W. Yu, Material and Solar Cells, *Coatings*, 2018, **8**, 304.
50 S. Giraldo, M. Neuschitzer, T. Thersleff, S. Lõpez-Marino, Y. Sánchez, H. Xie, M. Colina, M. Placidi, P. Pistor, V. Izquierdo-Roca, K. Leifer, A. Pérez-Rodríguez and E. Saucedo, *Adv. Energy Mater.*, 2015, **5**, 1501070.
51 S. Xiang, Y. Li, C. Xiang, H. Liu, Y. Zheng, S. Wang, W. Yan and H. Xin, *Phys. Chem. Chem. Phys.*, 2024, **26**, 20645–20652.
52 A. D. Collord and H. W. Hillhouse, *Chem. Mater.*, 2016, **28**, 2067–2073.
53 A. Crovetto, S. Kim, M. Fischer, N. Stenger, A. Walsh, I. Chorkendorff and P. C. K. Vesborg, *Energy Environ. Sci.*, 2020, **13**, 3489–3503.
54 G. Rey, G. Larramona, S. Bourdais, C. Choné, B. Delatouche, A. Jacob, G. Dennler and S. Siebentritt, *Sol. Energy Mater. Sol. Cells*, 2018, **179**, 142–151.
55 G. Rey, T. P. Weiss, J. Sendler, A. Finger, C. Spindler, F. Werner, M. Melchiorre, M. Hála, M. Guennou and S. Siebentritt, *Sol. Energy Mater. Sol. Cells*, 2016, **151**, 131–138.
56 M. Neuschitzer, Y. Sanchez, T. Olar, T. Thersleff, S. Lopez-Marino, F. Oliva, M. Espindola-Rodriguez, H. Xie, M. Placidi, V. Izquierdo-Roca, I. Lauermann, K. Leifer, A. Pérez-Rodriguez and E. Saucedo, *Chem. Mater.*, 2015, **27**, 5279–5287.
57 G. Rey, A. Redinger, J. Sendler, T. P. Weiss, M. Thevenin, M. Guennou, B. El Adib and S. Siebentritt, *Appl. Phys. Lett.*, 2014, **105**, 112106.
58 E. Isotta, B. Mukherjee, C. Fanciulli, N. M. Pugno and P. Scardi, *J. Phys. Chem. C*, 2020, **124**, 7091–7096.
59 S. Oueslati, M. Grossberg, M. Kauk-Kuusik, V. Mikli, K. Ernits, D. Meissner and J. Krustok, *Thin Solid Films*, 2019, **669**, 315–320.
60 Y. Atasoy, E. Bacaksız, A. Çiriş, M. A. Olğar, R. Zan, A. M. J. Al-dala Ali, T. Küçükömeroğlu and B. M. Başol, *Sol. Energy*, 2024, **267**, 112247.
61 S. Giraldo, M. Neuschitzer, T. Thersleff, S. Lõpez-Marino, Y. Sánchez, H. Xie, M. Colina, M. Placidi, P. Pistor, V. Izquierdo-Roca, K. Leifer, A. Pérez-Rodríguez and E. Saucedo, *Adv. Energy Mater.*, 2015, **5**, 1501070.
62 R. Scaffidi, G. Brammertz, Y. Wang, A. U. Zaman, K. Sasikumar, J. de Wild, D. Flandre and B. Vermang, *Energy Adv.*, 2023, **2**, 1626–1633.
63 S. Sahayaraj, G. Brammertz, B. Vermang, T. Schnabel, E. Ahlswede, Z. Huang, S. Ranjbar, M. Meuris, J. Vleugels and J. Poortmans, *Sol. Energy Mater. Sol. Cells*, 2017, **171**, 136–141.
64 M. Neuschitzer, J. Marquez, S. Giraldo, M. Dimitrievska, M. Placidi, I. Forbes, V. Izquierdo-Roca, A. Pérez-Rodriguez and E. Saucedo, *J. Phys. Chem. C*, 2016, **120**, 9661–9670.
65 M. Neuschitzer, M. E. Rodriguez, M. Guc, J. A. Marquez, S. Giraldo, I. Forbes, A. Perez-Rodriguez and E. Saucedo, *J. Mater. Chem. A*, 2018, **6**, 11759–11772.
66 J. Liu, Z. Liu, K. Gao, H. Cai, Y. Liu, W. Zhao, X. Liu, K. Cheng and Z. Du, *ACS Appl. Mater. Interfaces*, 2021, **13**, 56302–56308.
67 L. Sun, H. Shen, H. Huang, A. Raza, Q. Zhao and J. Yang, *Vacuum*, 2019, **165**, 186–192.
68 J. Wang, J. Zhou, X. Xu, F. Meng, C. Xiang, L. Lou, K. Yin, B. Duan, H. Wu, J. Shi, Y. Luo, D. Li, H. Xin and Q. Meng, *Adv. Mater.*, 2022, **34**, 2202858.
69 J. A. Clark, A. Murray, J. M. Lee, T. S. Autrey, A. D. Collord and H. W. Hillhouse, *J. Am. Chem. Soc.*, 2019, **141**, 298–308.
70 J. Fu, D. Kou, W. Zhou, Z. Zhou, S. Yuan, Y. Qi and S. Wu, *J. Mater. Chem. A*, 2020, **8**, 2229222301.
71 M. C. Baek, J. S. Jang, V. C. Karade, M. P. Suryawanshi, J. H. Kim, T. E. Hong, S. W. Park, S. W. Shin and J. H. Kim, *Chem. Eng. J.*, 2024, **479**, 147842.
72 X. Tan, J. Hu, W. Zhu, F. Wu and X. Han, *J. Alloys Compd.*, 2024, **981**, 173645.
73 L. Choubrac, M. Bär, X. Kozina, R. Félix, R. G. Wilks, G. Brammertz, S. Levcenko, L. Arzel, N. Barreau, S. Harel, M. Meuris and B. Vermang, *ACS Appl. Energy Mater.*, 2020, **3**, 5830–5839.
74 S. Kim, K. M. Kim, H. Tampo, H. Shibata and S. Niki, *Appl. Phys. Express*, 2016, **9**, 102301.
75 A. Ruiz-Perona, Y. Sánchez, M. Guc, S. Khelifi, T. Kodalle, M. Placidi, J. M. Merino, M. León and R. Caballero, *Sol. Energy*, 2020, **206**, 555–563.
76 G. M. Ford, Q. Guo, R. Agrawal and H. W. Hillhouse, *Chem. Mater.*, 2011, **23**, 2626–2629.
77 F. Urbach, *Phys. Rev.*, 1953, **92**, 1324.

